Native and radiation induced point defects in AlN and Sc-doped AlN

Yuri Osetsky,[1,*] Mao-Hua Du,[1] German Samolyuk,[1] Steven J. Zinkle,[1,2] and Eva Zarkadoula[1,†]
[1]*Materials Science and Technology Division, Oak Ridge National Laboratory, Oak Ridge, Tennessee, USA*
[2]*University of Tennessee, Knoxville, Tennessee, USA*

(Received 12 December 2021; revised 18 April 2022; accepted 19 July 2022; published 15 September 2022)

We have performed first-principles calculations to investigate the electronic structure, configurations, formation, and binding energies of native and radiation induced point defects in pristine and Sc-doped wurtzite AlN. For the native defects, the nitrogen vacancy has the lowest formation energy in *p*-type material while the aluminum vacancy has the lowest formation energy in *n*-type material which is consistent with the previous studies. Several interstitial defect structures were modeled for Al, N, and Sc atoms. The effects of charge state on their relative stability were investigated. The binding energy of Sc with point defects was calculated and found to be dependent strongly on the defect type and charge state. The results obtained are discussed in light of the possible Sc effects on the radiation damage evolution in AlN. Thus the attraction of Sc atom to N vacancy and both Al and N interstitials reduces their mobility and increases Frenkel pair recombination distance.

DOI: 10.1103/PhysRevMaterials.6.094603

I. INTRODUCTION

AlN is one of the group-III nitride materials with a wide band gap that are being intensively studied because of their outstanding properties in many applications. Thus, wurtzite AlN is extensively used in optoelectronic, photonic, and piezoelectric devices [1–4]. It was recently shown that it exhibits amazing properties in forming solid state qubits [4,5]. Because of its good radiation damage tolerance [6], it has a very promising potential as a functional material for sensors in nuclear devices subjected to harsh environments. Previous studies showed that AlN provides very good radiation tolerance for piezoelectric properties and high temperature stability [6–8]. It was shown that the piezoelectric properties of AlN are unaffected by gamma radiation up to 26.8 MGy and by fast neutron fluence of 1.85×10^{18} n/cm^2 and thermal neutron fluence 5.8×10^{18} n/cm^2 [9]. Additionally, it has been shown [10,11] that AlN-based transducers maintain their piezoelectric response during the entire irradiation (neutron fluence 8.65×10^{20} n$_f$/cm^2 and gamma fluence 7.23×10^{21} gamma/cm^2 at 420 °C) and perform better than other candidate ceramics such as ZnO and BiTiO3 [11]. The ability to retain its piezoelectric response during irradiation, in combination with the overall good radiation response of AlN, makes it a candidate material for piezoelectric sensing technologies for advanced nuclear reactors [12]. However, the piezoelectric coefficient of AlN is low (about 5 pm/V) compared to the coefficients of some other ceramics (such as 10 pm/V for zinc oxide and 18 pm/V for bismuth titanate [12]). Recent studies have shown that alloying AlN with metals, such as scandium (Sc), improves the piezoelectric response by up to 40% [13–18] making these materials very attractive for practical usage.

Properties of pure and doped AlN, relevant to its unique applications, are defined mostly by their band structure; thus first- principles approaches have been intensively applied. Pristine AlN and AlN containing dopant impurities, including gases and elements from groups II, IV A, and IV B, were investigated using the density functional theory (DFT) based calculations, for example, in [4,5,19,20]. However, very limited information can be found on doping with Sc. Moreover, previous studies were focused mainly on optoelectronic and magnetic applications whereas piezoelectric applications under irradiation conditions have not been considered so far. Recent applications of AlN as sensors in nuclear devices demand knowledge of radiation damage mechanisms for predicting their lifetime. Neutron and ion irradiation experiments have provided important insights into the radiation response of AlN. A number of radiation effects are reported such as swelling [21–23], loss of thermal conductivity [24–27], and growth of interstitial loops [23,28,29]. Thus, swelling associated with introduced gas, i.e., oxygen or helium, was observed in [21,22]. The high density of small interstitial-type dislocation loops, $\leqslant 5$ nm in diameter, was reported after neutron irradiation [23,28,29]. Loops are preferentially formed in the basal plane and cause a macroscopic volume change due to corresponding elastic strain (not associated with vacancy voids). AlN has been observed to exhibit good resistance to radiation induced disordering compared to GaN or $Al_xGa_{1-x}N$ [30]. In general, AlN ceramics demonstrate significant resistance against radiation damage although more work needs to be done to achieve a clear understanding of the governing mechanisms.

There are very few reported attempts in describing the fundamentals of high radiation tolerance of AlN. Some radiation damage effects in ceramic materials are discussed in a recent review [29]. Among the discussed effects, one key

*osetskiyyn@ornl.gov
†zarkadoulae@ornl.gov

contribution might be that the onset of interstitial migration in AlN apparently occurs at $T < 80$ K on both the anion and cation sublattice [28,31]; this underlines the importance of understanding interstitial properties. Recent work on low-energy primary radiation damage in wurtzite AlN was studied by *ab initio* molecular dynamics (AIMD) modeling of Frenkel pairs (FPs) formation [32]. High orientational anisotropy in threshold displacement energy was observed; i.e., Frenkel pair creation is easier for primary knocked-on atoms (PKAs) displaced along the direction parallel to the basal planes. The minimum threshold energy was determined along with the directions as 19 eV for Ni-type FP (N FP) and 55 eV for Al-type FP (Al FP). The corresponding energies for the PKAs displaced along the [0001] direction were determined as >39 and >94 eV, respectively. It was reported that the FPs formed in these recoil events modify the electronic structure forming new localized states within the band gap. As far as doping with Sc is concerned, more information on Sc effects on defects in AlN and its contributions to radiation effects is needed.

In the present paper, we address this gap. We studied the formation energy of native defects in pure AlN and compared them with the previous results. A detailed investigation was performed for interstitial defect, their atomic structure, and interaction with the Sc-dopant atom. Last, we discuss the next approaches toward the understanding of radiation damage of these materials.

II. METHODS

A. Modeling approach

Electronic structures and energies have been calculated within the density-functional theory [33] using the generalized gradient approximation (GGA) and the Perdew-Burke-Ernzerhof (PBE) [34] parametrization of the electronic exchange-correlation functional. Total energies and electronic structure were calculated using the plane-wave basis projector augmented-wave approach [35] as implemented in the Vienna *ab initio* simulation package (VASP) [36]. A plane-wave energy cutoff of 350 eV and $2 \times 2 \times 2$ k mesh were used to obtain defects formation energy in a $3 \times 5 \times 3$ supercell containing 360 lattice sites, where the repeating unit corresponds to a minimal possible rectangular cell of wurtzite-type AlN structure. Initially, in the perfect system c/a ratio, shape, volume, and atomic positions were relaxed until the total pressure dropped below 0.1 kbar and forces acting on atoms do not exceed 10^{-5} eV/A. As a result, we have obtained a perfect wurtzite lattice with parameters $a = 3.128$ Å and $c = 5.015$ Å, $c/a = 1.603$ ratio (see Fig. 1). This is in good agreement with calculated and experimental data [37–41] that include bond lengths between atoms in the c plane, Al-N_{in}, and normal to it, Al-N_{out}, and angles between the corresponding bonds such as α_{in}-in between two Al-N_{in} bonds and α_{in}-out between Al-N_{in} and Al-N_{out} bonds as seen in Table I. We also calculated the heat of formation of AlN and ScN that was equal to $\Delta H_{AlN} = -3.203$ eV and $\Delta H_{ScN} = -4.224$ eV per the corresponding molecule; these are quite similar to the experimentally derived energies –3.28 eV [42] and α_{in-in} 4.56 eV [43], correspondingly. This ensures the realistic stability of the corresponding phases modeled here. During the further modeling of defects, the shape and volume of the supercell were kept constant and atomic positions were optimized until the maximum force on atoms dropped <0.01 eV/Å.

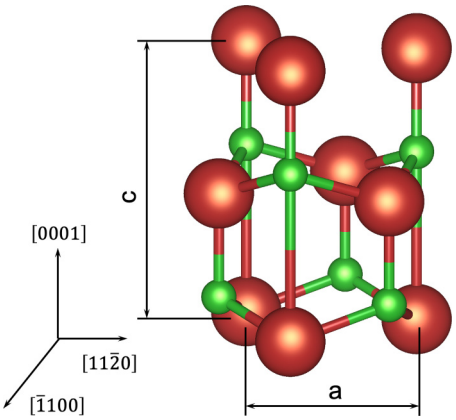

FIG. 1. Atomic structure of wurtzite AlN crystal (Al: red; N: green).

B. Defects formation and binding energies

Within supercell defect formalism, the formation energy, $E_D^f(q)$, of a defect D is expressed as

$$E_D^f(q) = E_{\text{defect}}^{\text{tot}}(q) - E^{\text{tot}}(\text{bulk}) - n_{\text{Al}}\mu_{\text{Al}} - n_{\text{N}}\mu_{\text{N}} + q(E_v - E_F) + E_{\text{corr}}, \quad (1)$$

where $E_D^{\text{tot}}(q)$ is the total energy of the supercell containing the defect in the charge state q, $E^{\text{tot}}(\text{bulk})$ is the total energy

TABLE I. Properties of the wurtzite crystal modeled here, derived experimentally [37–39] and calculations reported in other references. Units are angstroms for length and degrees for angles.

	a	c	c/a	Al-N_{in}	Al-N_{out}	α_{in}-out	α_{in}-in
This work	3.128	5.015	1.603	1.901	1.914	108.2	110.7
Other calculations	3.174[a]	5.107[a]	1.609[a]				
	3.118[b]	5.041[b]	1.616[b]				
	3.130[c]	5.020[c]	1.604[c]				
Experiment	3.110	4.980	1.601	1.889	1.903	110.8	108.9

[a]Calculations reported in Ref. [32].
[b]Calculations reported in Ref. [40].
[b]Calculations reported in Ref. [41].

of a perfect supercell, n_{Al} and n_N are the numbers of Al and N atoms added to or taken from the bulk crystal in order to create the considered defect, and μ_{Al} and μ_N are the corresponding chemical potentials. E_v represents the energy at the valence-band maximum of the defect-free system. E_F is the Fermi energy relative to E_v. Finally, $E_{corr} = \Delta E_{MP} + \Delta E_{bf} + \Delta E_{pa}$ contains the set of finite modeling cell size corrections, i.e., the image charge corrections ΔE_{MP}, [42–44] and the Moss-Burstein-type band-filling corrections, ΔE_{bf}, [45,46], and the potential-alignment energy correction for the supercell with a net charge, ΔE_{pa} [43,44]. The image charge correction for the $3 \times 5 \times 3$ supercell, obtained using the calculated value of static dielectric constant ε_0, 8.709, is $0.1q^2$ eV. The sum of band-filling and potential-alignment corrections, $\Delta E_{bf} + \Delta E_{pa}$, is found to be dependent on the defect type and its charge state. For example, for the Al vacancy, V_{Al}, it varies from –0.14 to –0.07 eV when the charge varies from –3 to 0 considered here for this defect (see Table III). For the Al interstitial atom, $I1_{Al}$, i.e., $\langle 11\bar{2}1\rangle$-dumbbell (*d-b*), this varies from 0.06 to 0.13 eV for the considered charges from 0 to +3. This correction is quite small at the neutral state and has its maximum value at the maximal considered charge states. Sc substitution in the Al site is the only defect having a significant correction at the neutral state: $\Delta E_{bf} + \Delta E_{pa} =$ –0.15 eV. These are extreme cases, where the band-filling and potential-alignment corrections are maximal. In general, band-filling and potential-alignment corrections contribute at the lowest charge states, whereas ΔE_{MP}, following the charge square dependence, dominates at charged states above ± 1. In general, E_{corr} described here is important for native defects; because of their relatively low formation energies, small deviations affect their equilibrium concentrations. Radiation induced defects are not formed thermodynamically but are due to ballistic interactions. Microstructure evolution under irradiation is mainly affected by defect interaction and binding whose energies are less affected by the above corrections.

Calculations were also performed to evaluate defect property changes due to the Sc dopant. The binding energy of a defect D and Sc atom, $E^b_{D-Sc}(D\text{-Sc})$, can be defined as

$$E^b_{D-Sc} = E^f_D + E^f_{Sc_{Al}} - E^f_{D-Sc}, \tag{2}$$

where E^f_D and E^f_{D-Sc} are the minimum values of the corresponding defect formation energies in pure and Sc-doped AlN calculated via Eq. (1) for the same charge conditions. Each individual energy in Eq. (2) accounts for the finite modeling cell size corrections and, therefore, the resulting D-Sc binding energy also includes these effects explicitly. It is important that E^b_{D-Sc} is charge dependent and, in general, can be related to the different defects' configurations following their relative stability.

Estimation of chemical potential values in compounds is an issue affecting the accuracy of the estimated defect formation energies. This is especially important in semiconductors, where the conditions for phase stability of the matrix, its constituent elements, and doping atoms should be taken into account. Here we consider equilibrium conditions for the AlN crystal growth from free Al and N_2. Chemical potentials for Al, N, and Sc in the AlN compound were determined following the assumptions and procedure described recently in [47]. The following constraints were applied to ensure the stability of AlN and Sc-doped AlN phases: $\mu_{Al} + \mu_N = \mu_{AlN}$ and $\mu_{Sc} + \mu_N \leqslant \mu_{ScN}$. Here μ_{AlN} and μ_{ScN} are enthalpies of formation of AlN and ScN estimated by modeling the corresponding perfect crystals. The first constraint provides Al and N in thermal equilibrium with AlN, whereas the second one prevents the formation of the ScN phase in AlN. Furthermore, the chemical potentials must satisfy the boundary conditions $\mu_N \leqslant 1/2\mu_{N_2}$ and $\mu_{Al} \leqslant \mu_{Al(bulk)}$ (if this is not the case, then AlN would be thermodynamically unstable with respect to the formation of N_2 molecules or bulk Al). In the application to the AlN matrix, one may consider nitrogen-rich (N-rich) or aluminum-rich (Al-rich) conditions. Then, at N-rich conditions $\mu_N = 1/2\mu_{N_2}$, $\mu_{Al} = \mu_{AlN} - \mu_N$, and $\mu_{Sc} = \mu_{ScN} - \mu_N$ whereas at Al-rich conditions $\mu_{Al} = \mu_{Al(bulk)}$ and $\mu_N = \mu_{AlN} - \mu_{Al}$, and $\mu_{Sc} = \mu_{ScN} - \mu_N$. The values of all chemical potentials used here for estimating defect formation energies are listed in Table II.

TABLE II. Chemical potentials (in eV) used for calculation defect formation energies under N- and Al-rich conditions.

	μ_{Al}	μ_N	μ_{Sc}
N-rich	–6.947	–7.955	–10.555
Al-rich	–3.744	–11.158	–7.325

III. RESULTS

A. Electronic structure

The densities of states (DOS) for the perfect AlN supercell and that with relaxed N and Al vacancies and Sc in Al substitution are presented in Fig. 2. As seen here, the calcutaed band gap is 4.1 eV, which is underestimated compared to the measured value of 6.12 eV [48]. It can be seen that defects affect the DOS. The Al vacancy shifts the whole density of states slightly toward lower values of the Fermi energy, whereas the DOS shifts significantly, by the whole bandwidth, in the case of the N vacancy. Sc substituting for the Al atom provides a negligible modification to the DOS. Similar to previously published results [19], we found that a vacancy in the Al site leads to the formation of triplet states at the bottom of the gap occupied by three electrons, while the nitrogen vacany forms two states occupied by two electrons right above the valence band and a triplet state at the top of the gap close to the conduction band containing one electron. Substitution of Al by one isoelectronic Sc atom does not result in information of any new states. The observed underestimation of the band gap is typically observed in the traditional density functional approach [20]. This challenge can be addressed by utilizing either the *GW* [49] or the hybrid functional (HF) [5,50] approaches to accurately incorporate exchange-correlation effects. A comparison of different techniques for the band gap estimations is presented in the Ref. [51] and it was concluded that more complicated techniques, such as *GW*, are likely to provide better results on the electronic structure than DFT-based methods. However, the defect formation energies are not significantly different. The latter properties are of main importance in the current work addressing the Sc-doping

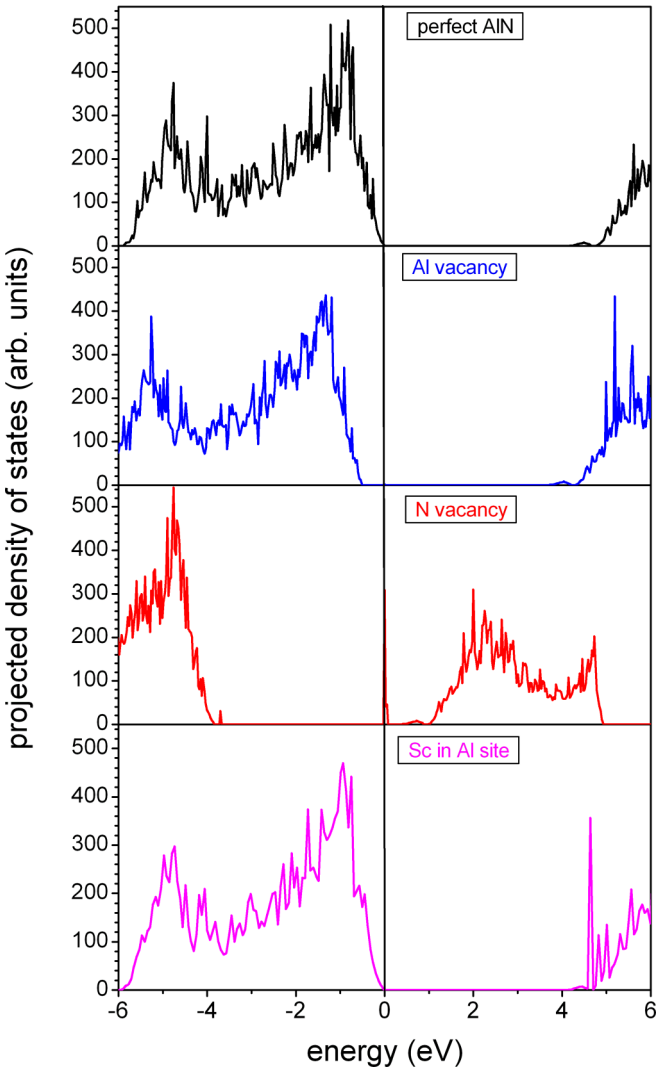

FIG. 2. Density of states for the perfect AlN supercell and including some native defects.

effects on the defects' energetics. Moreover, the complexity of the *GW* and HF calculations makes them hardly applicable to large supercell calculations while calculation of defect properties in small supercells results in errors that exceed the errors from an underestimated band gap value. This effect is important for interstitial defects that, in general, need larger supercells than vacancy and substitution defects. The modeling approach used here allows us to model supercells larger than previously reported studies that we consider preferable for radiation defects study.

B. Point defects in the pristine and Sc-doped AlN

Defects in materials can be formed in different ways, such as temperature, deformation, and irradiation by energetic particles. Defects formed due to permanent ambient conditions, such as temperature, are native and coexist at thermodynamic equilibrium. These defects are important for understanding properties and evolution under equilibrium or relaxation toward equilibrium conditions such as diffusion, segregation, and phase transformations. As native defects we consider here vacancies in both Al and N sites (noted as V_{Al} and V_N, respectively), antistites that are Al in N sites (noted as Al_N), and N in Al sites (noted as N_{Al}), and Sc substitution in Al and N sites (noted as Sc_{Al} and Sc_N). Native defects are expected to be formed during material fabrication and their concentration depends on the equilibrium conditions considered. To estimate these correctly, defect energies need to be calculated for the applicable charge states and their minima should be used for thermodynamic equilibrium estimations. The possible charge states for the native defects in AlN were discussed in [19] and are used here for formation energy calculations. Doping by Sc atoms in the Al sites does not introduce new gap states and thus we have considered only the neutral charge state for Sc_{Al}.

Under irradiation conditions defects are formed due to ballistic effects and their evolution does not follow thermodynamic equilibrium conditions. Moreover, the charge states of primary damage defects, such as vacancy and interstitial atoms and their small clusters, are unidentified, and probably depend on the irradiation conditions for ions, electrons, and neutrons, combined with bulk and local composition. Interstitial atoms are typical examples of radiation induced defects and were not considered previously among the native defects for equilibrium conditions because of their high formation energy. Very limited information on interstitial atoms in AlN has been reported so far: The considered N interstitial atom configurations are octahedral and tetrahedral in [19,20,32] and a tilted $\langle 11\bar{2}0\rangle$-dumbbell in [32]. Like other hexagonal lattices, wurtzite produces several structurally stable configurations for both Al (I_{Al}) and Ni (I_N) interstitial atoms that may play a role in their mobility under irradiation conditions and thus should be investigated. For example, in hcp Zr the interstitial atom migration mechanism involves multiple transitions between different configurations [52,53]. Interstitial defects were studied here, and several configurations of N, Al, and Sc interstitials and their structure are described below.

Not much information is known on the real defect charge states in AlN at irradiation conditions. Limited information is available on the vacancy-type defects in [54], where annealing of the optical absorption and electron spin resonance was studied after neutron irradiation. F and F^+ center, i.e., N vacancies that may trap one or two electrons, were observed. In our calculations, we considered charge states for different defects depending on their ability to capture or give electrons as discussed in [19]. Table III contains defect acronyms and short descriptions, considered charge states, and energy of neutral defects presented for general information and qualitative comparison of different configurations. Some details on the structure and energy properties are presented in the following sections: the structure of point defects in Sec. III B 1, charge dependence of the formation energy of substitution, vacancy and interstitial defects in AlN in Sec. III B 2, the effect of Sc doping on the defect energy properties in Sec. III B 3, and the Sc-doping effect on structure and energy of Frenkel pairs in Sec. III B 4.

1. *Structure of point defects in the pristine and Sc-doped AlN*

Native defects such as vacancies and antistites usually relaxed into structurally stable configurations with a weak relaxation of surrounding atoms except, possibly, the Al in N

TABLE III. Abbreviation, charge state of all the defects considered, and their formation energy obtained after relaxation at a neutral charge state. For complexes of two defects, "in" and "out" mean that defects are at the nearest neighbors in the same or different (0001) planes, respectively.

Abbreviation	Charge states considered	Defect description		Formation energy (eV) Al-rich	N-rich
V_{Al}	–3, –2, –1 0	Vacancy in Al site		9.79	6.59
V_N	+1, +2, +3	Vacancy in N site		3.29	6.49
Al_N	–1, 0, +1, +2, +3	Al substitution in N site		14.73	8.61
N_{Al}	–1, 0, +1, +2	N substitution in Al site		6.59	12.70
I_{Al}	0, +1, +2, +3	Al interstitial atom	$I1_{Al}$l:$\langle 11\bar{2}1\rangle$ *d-b*	12.61	9.70
			$I2_{Al}$:$\langle 11\bar{2}0\rangle$ *d-b*	14.02	11.11
			$I3_{Al}$:$\langle 10\bar{1}0\rangle$ *d-b*	14.15	11.24
			$I4_{Al}$: O	12.90	9.99
I_N	–1, 0, +1	N interstitial atom	$I1_N$: $\langle 11\bar{2}1\rangle$*d-b*	7.71	4.51
			$I2_N$: T	8.50	5.30
Sc_{Al}	0	Sc atom substitution in Al site		1.03	1.95
Sc_N	–1, 0, +1, +2, +3	Sc atom substitution in N site		16.53	22.96
Sc+Sc	0	2 Sc atoms in Al sites	In	2.26	2.32
			Out	2.14	2.19
Sc+vacancy	–3, –2, –1, 0	$Sc_{Al} + V_{Al}$	In	11.26	8.08
			Out	10.94	7.76
	0, +1, +2, +3	$Sc + V_N$	In	2.488	
			Out	2.236	
Sc+interstitial atom	0, +1, +2, +3	$Sc + I_{Al}$	$I1_{Sc}$: $I_{Sc\text{-}out}$	9.985	
			$I2_{Sc}$: $Sc_{Al} + I4_{Al}$	9.112	
	–1, 0, +1	$Sc + I_N$	$Sc_{Al} + I1_N$	7.258	0.851
			$Sc_{Al} + I2_N$	8.411	2.005

site substitution that provoked significant atomic distortions, being nevertheless structurally stable. This configuration has quite a high formation energy $E^f = 14.73$ eV (hereinafter, for brevity, we compare only Al-rich conditions; values for N-rich conditions can be found in Table III).

Interstitial atoms are more complicated defects because of the variety of their configurations and their highly asymmetric character. Four structurally stable Al interstitial atom configurations are presented in Fig. 3. Figure 3(a) shows the configuration that can be described as a dumbbell along close to the $[11\bar{2}1]$ direction, denoted as $I1_{Al}$ in Table III. The distance between dumbbell atoms $d = 2.21$ Å and the formation energy at the neutral charge state $E^f = 12.605$ eV. One can see the left Al atom has three Al-N bonds whereas the right atom has only two Al-N bonds. Another dumbbell configuration in the $(\bar{1}100)$ plane split along the $\langle 11\bar{2}0\rangle$ direction is shown in Fig. 3(b) ($I2_{Al}$ in Table III). In this dumbbell Al atoms are closer to each other: $d = 2.18$ Å, but the neutral charge formation energy is higher: $E^f = 14.02$ eV, while Al-N bonds are distributed in the same way as for the above $I1_{Al}$ configuration. A symmetric dumbbell in the (0001) plane along the $\langle 10\bar{1}0\rangle$ direction is shown in Fig. 3(c) ($I3_{Al}$ in Table III). This configuration is characterized with $d = 2.24$ Å, $E^f = 14.15$ eV, and both dumbbell atoms have three Al-N bonds each. The most stable orientation, at neutral charge state, was found to be a slightly asymmetric octahedral configuration shown in Fig. 3(d) ($I4_{Al}$ in Table III). The interstitial Al atom relaxed at the distance 1.35 Å from the N plane and 1.41 Å from the Al plane with formation energy $E^f = 9.70$ eV and three equal length Al-N bonds: $d_{Al-N} = 1.87$. Note that d_{Al}-N = 1.94 Å in the perfect AlN crystal. The globally stable configuration of a neutrally charged Al interstitial depends on the conditions: At Al-rich conditions it is an octahedral interstitial, whereas the most stable configuration at N-rich conditions is the $[11\bar{2}1]$ dumbbell as seen in Table III.

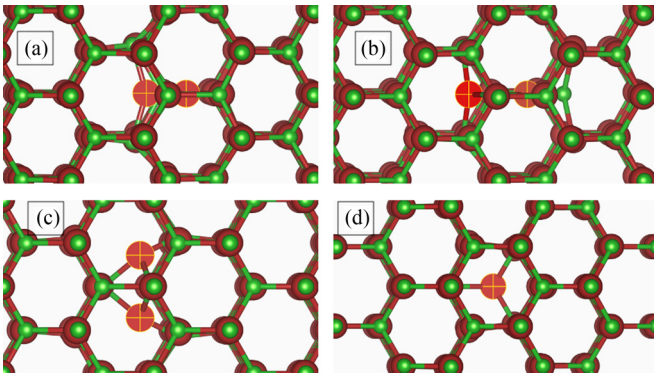

FIG. 3. Neutral charge state configurations of Al interstitial atom (crossed) projected onto the (0001) plane: (a) dumbbell in $(\bar{1}100)$ plane along close to the $\langle 11\bar{2}1\rangle$ direction; (b) dumbbell in the $(\bar{1}100)$ plane along the $\langle 11\bar{2}0\rangle$ direction; (c) dumbbell in the (0001) plane along the $\langle 10\bar{1}0\rangle$ direction; (d) octahedral configuration with a slight asymmetry.

Two structurally stable configurations were found for the N interstitial atoms. They were relaxed from initial tetrahedral or octahedral positions, but their final configurations are neither

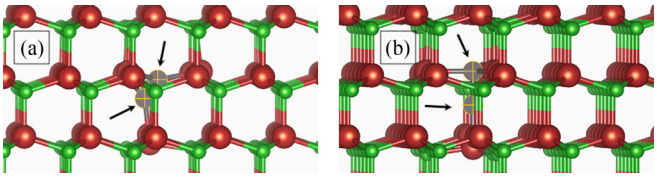

FIG. 4. Neutral charge configurations of N interstitial atom (gray crosses indicated by arrows) projected onto $(11\bar{2}0)$ plane initially inserted into (a) octahedral or $\langle 11\bar{2}0\rangle$ dumbbell, and (b) tetrahedral configuration and relaxed at the neutral charge states.

of these two as can be seen in Fig. 4. The N interstitial atom initially inserted into the octahedral or $\langle 11\bar{2}0\rangle$-dumbbell position has relaxed into a N-N dumbbell oriented along the $\langle 11\bar{2}1\rangle$ direction with the distance between the N atoms being $d_{\text{N-N}} = 1.40$ Å [see Fig. 4(a)]. The initially created N interstitial in the tetrahedral position has relaxed into a N-N dumbbell oriented exactly along the [0001] direction with a distance between N atoms of $d_{\text{N-N}} = 1.38$ Å [see Fig. 4(b)]. The main difference of this configuration from the regular tetrahedral interstitial is preferential relaxation of atoms along the [0001] direction, whereas the tetrahedral configuration assumes three-dimensional relaxation of all the surrounding atoms. The $\langle 11\bar{2}0\rangle$ dumbbell is more stable than the tetrahedral configuration for both Al- and N-rich conditions as seen in Table III.

When doping, the simplest defect is Sc replacement of the Al atom: It is structurally stable and has a low formation energy. Two neighboring Sc replacements of Al atoms can form two configurations either in the same or different (0001) planes. Both are stable defects with very similar energies as can be seen in Table III. On the contrary, Sc replacement of N atoms leads to a significant relaxation when two atoms, Sc inserted into the N position and the closest Al, move significantly from their initial positions as shown in Fig. 5. The distance between the marked Sc and Al atoms is $d_{\text{Sc-Al}} = 2.25$ Å, compared with the equivalent distance in perfect crystal $d_{\text{N-Al}} = 1.91$ Å (see Table III). For the Sc interstitial, we have observed only two stable symmetric configurations. Sc in the octahedral position has the formation energy $E^f = 9.99$ eV (I1_{Sc} in Table III) whereas a configuration where Sc replaces an Al atom that is pushed out to the octahedral configuration has a lower neutral state energy $E^f = 9.11$ eV (I2_{Sc} in Table III). Both configurations are similar to that shown in Fig. 3(d) with the only difference being the I1_{Sc} Sc atom is in the octahedral position atoms whereas for I2_{Sc} one of the closest to octahedral atom Al sites is occupied by Sc.

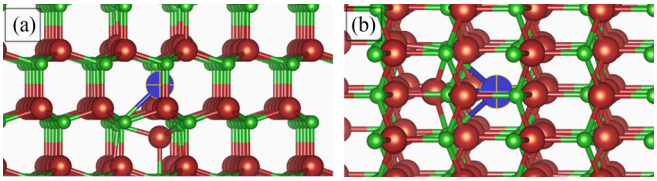

FIG. 5. Relaxed neutral charge configuration of Sc atom (blue crossed) substituting N projected onto (a) $(\bar{1}100)$ and (b) $(11\bar{2}0)$ planes.

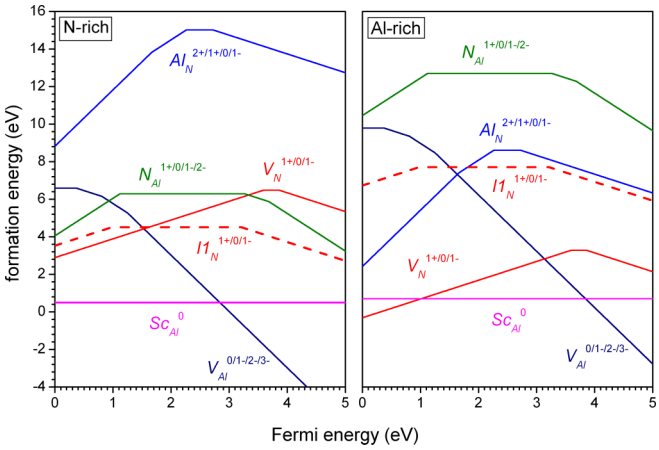

FIG. 6. Formation energy of native defects in AlN as function of Fermi energy under N- and Al-rich conditions. Only the lowest energy segments are indicated for a particular charge state. Defect abbreviations and considered charges are explained in Table III.

2. *Energy of charged defects in AlN*

The formation energies of native defects as functions of Fermi energy E_F are presented in Fig. 6, for N- and Al-rich conditions. The Fermi energy was varied within a range slightly wider than the band gap width, i.e., 5 eV instead of 4.1 eV, to show their behavior near the band gap maximum. For each defect, we present only the segment of the whole charge state dependence related to the minimum energy among the other states at the current E_F level. Due to its relatively low formation energy and previous studies [19,20], we also included a N interstitial in configuration I1_{N} among the native defects.

Radiation may induce interstitial defects and, therefore, here we considered two N interstitials and four Al interstitials whose structures are shown in Figs. 3 and 4 for the neutral state. Since each defect may have different charge states the total picture looks quite complicated and the relative stability of different defects depends strongly on E_F. Moreover, defect stability is quite different for the N- and Al-rich conditions considered here. The most stable defects are vacancies; thus V_{Al} may have very low formation energy when negatively charged. The structure of vacancies does not depend on their charge state; the charge state only slightly affects the length of local bonds. Another relatively stable defect is the N interstitial atom in the configuration denoted as I1_{N} in Table III. However, the detailed structure of this defect depends on its charge state as can be seen in Fig. 7. Thus, at $q = +1$ [Fig. 7(c)] its structure is similar to that at the neutral state [compare with that in Fig. 4(a)]. At $q = -1$ it changes from the $\langle 11\bar{2}1\rangle$ dumbbell to the $\langle 10\bar{1}0\rangle$ dumbbell, which now lies exactly in the (0001) plane as seen in Figs. 7(a) and 7(b). As a result, I1_{N} can be quite stable near both valence band maximum (VBM) and conduction band minimum (CBM), especially at Al-rich conditions.

Additional interstitial atom configurations in AlN were investigated at different conditions; the results on their formation energy are presented in Fig. 8. A positively charged Al interstitial can be stable near the VBM, whereas all of them

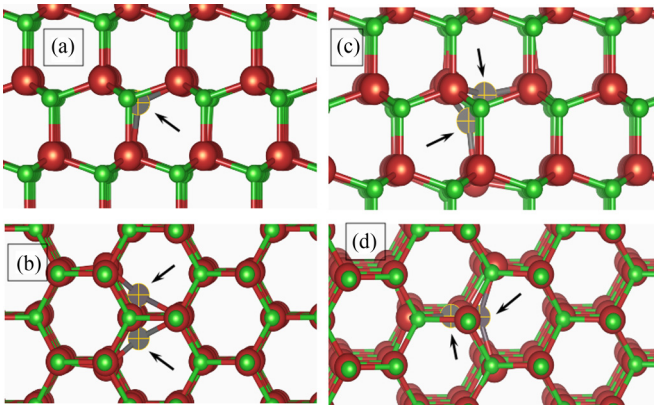

FIG. 7. Structure of N interstitial atom (gray crossed spheres indicated by arrows) in configuration $I1_N$, at different charge states: (a), (b) $q = -1$; (c), (d) $q = +1$, projected onto different planes: (a), (c) $(11\bar{2}0)$ plane; (b), (d) (0001) plane.

have very high formation energy near the CBM. Importantly, the difference in formation energy of different interstitial defects of the same type is insignificant and sometimes their relative stability changes depending on the Fermi energy.

Assuming the variety of particular conditions between Al-rich and N-rich limiting cases, one can suggest that the defects shown in Fig. 8, except antisites Al_N and N_{Al}, can be present in the AlN system under certain thermodynamical equilibrium and charge conditions and, thus, could be considered as native defects.

3. Energy of defects in Sc-doped AlN

Formation energies of the most stable interstitial defects in the pristine and Sc-doped AlN crystals as a function of Fermi energy are presented in Fig. 9. Data for the pristine AlN, solid lines, are presented for a visual demonstration of how the defect's relative stability can be changed depending on the charge state and fabrication conditions (i.e., N-rich or Al-rich): Sc doping, shown by dashed lines, can either increase or decrease the defect formation energy, introducing a quite overall complicated effect.

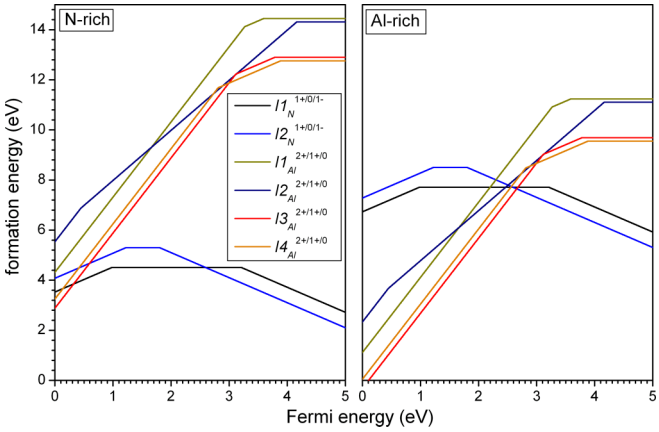

FIG. 8. Formation energy of interstitial point defects in AlN as function of Fermi energy under N- and Al-rich conditions.

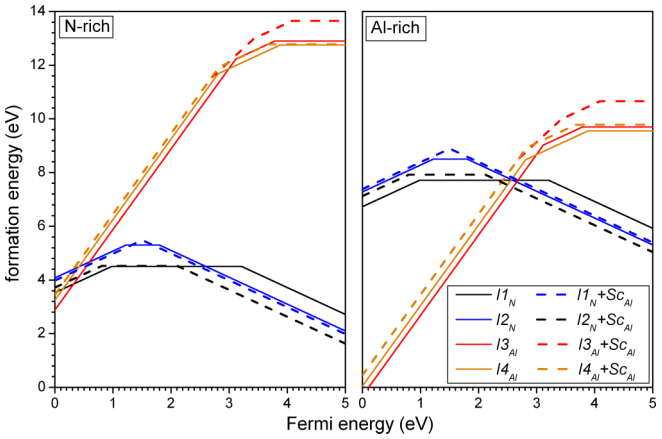

FIG. 9. Formation energy of interstitial defects in the pristine and Sc-doped AlN as function of Fermi energy under N- and Al-rich conditions. Defect's abbreviations are explained in Table III.

Among all energy properties, the most accurate calculations are for binding energies because according to Eq. (2) all chemical potentials can be eliminated and the binding energy value can be expressed as a combination of the relaxed energies of the corresponding configurations. In calculating Sc-dopant binding energy with the particular configuration, we always considered Sc substitution of the Al atom closest to the defect. The Sc-defect binding energy was calculated using the formation energies of the separate defect (E_D^f) and Sc atom ($E_{Sc_{Al}}^f$) and Sc-defect complex (E_{D-Sc}^f) taken from Figs. 8 and 9 and Table III, according to Eq. (2). The resulting behavior of E_{D-Sc}^b (F_F) varies for different defects as seen in Fig. 9. Thus Sc-Sc interactions demonstrate charge-independent weak repulsion, –0.09 eV [two Sc atoms in the same (0001) plane, i.e., Sc+Sc in] and –0.22 eV [two Sc atoms are in different (0001) planes, i.e., Sc+Sc out], that should lead to a low probability of their precipitation. The Al vacancy repels a Sc atom and its initially negative binding energy decreases more toward the CBM level. Nitrogen vacancy has a weak attraction with Sc dopant $E_{V_N-Sc}^b \sim 0.1$ and ~ 0.3 eV when they are in different and the same (0001) planes, respectively, with a narrow strong binding $E_{V_N-Sc}^b \sim 1.0$ near the VBM. Interstitials have attractive interaction with Sc with the different effects of the Fermi level. Binding energy with N interstitials increases at higher Fermi levels up to >1 eV, whereas that for Al interstitials increases only up to ~0.3–0.5 eV. We have found that the Sc dopant may change the interstitial configuration structure. For example, as discussed above $I1_N$ may change configuration depending on the charge state, and the most stable is the $\langle 10\bar{1}0\rangle$ dumbbell charged with $q = -1$ [see Fig. 10(a)]. However, the presence of a Sc atom at the same charge state changes the configuration back to the $\langle 11\bar{2}1\rangle$ dumbbell [see Fig. 10(b)], similar to that observed at the neutral state [see Fig. 3(a)].

4. Frenkel pairs in Sc-doped AlN

The Frenkel pair (FP) is a basic radiation induced defect formed at the primary damage stage due to collision effects. In the AlN system two types of FPs can be considered: Al FP consists of a vacancy at an Al site and an Al interstitial atom,

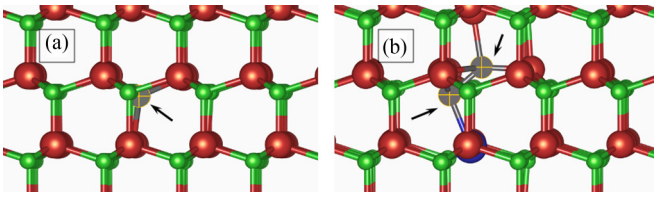

FIG. 10. Configurations of N interstitial atom $I1_N$ (crossed gray spheres indicated by arrows) charged with $q = -1$ and projected onto the $(11\bar{2}0)$ plane: (a) in pure AlN; (b) with Sc substitution in the nearest Al site (blue sphere).

and N FP that consists of a N vacancy and interstitial atom. Interstitial configurations considered were $I4_{Al}$ (octahedral) for Al FP and $I1_N$ ($\langle 11\bar{2}1\rangle$ dumbbell) for the N FP. Depending on the irradiation conditions, FPs with different separation, d_{FP}, between the constituent defects are formed and those with a short d_{FP} usually recombine within a short time after the collision event. Widely separated FPs behave as isolated vacancies and interstitials and the Sc-dopant effect can be estimated correspondingly, e.g., using data from Fig. 10. We observed that defects in the first two coordination spheres were unstable and recombined during relaxation. The closest stable Al and N FPs modeled here have $d_{FP} \approx 3.7$–3.8 Å whereas the widest investigated separation, $d_{FP} \approx 11.0$–11.5 Å, was limited by the supercell size used here. The effect of doping with Sc was estimated for the maximally separated FP of each type by substituting an Al atom, close to the center of the line between FP defects, by a Sc atom. The Sc FP binding energy calculated via Eq. (2) was found to be negative for Al FP, $E^b_{FP-Sc}(FP + Sc) + -0.246$ eV, and positive for N FP, $E^b_{FP\text{-}Sc}(FP + Sc) = +0.105$ eV. The repulsion from the Al FP and attraction to the N FP can be qualitatively understood if one takes into account the results for Sc binding with different defects presented in Fig. 10 above. While more configurations need to be modeled for a complete understanding of the Sc effect on FPs' stability the results presented here indicate clearly that Sc may affect the stability of FPs during irradiation.

IV. DISCUSSION

Formation energies of native defects reported in the literature were studied using different approaches. Thus, the plane wave based approach with exchange correlation considered in local density approximation (LDA) was used to model vacancies in [55]. Both LDA and GGA for the exchange-correlation functional were used in [19,56]. The FPLAPW method implemented in the WIEN2K package [57] was applied in [20] and the HSE06 screened hybrid functional was used to model N vacancy in [5]. The supercell size varied from 32 atoms in [19,57] and 72 atoms in [20] to 96 atoms in [5,58]. Overall, all the above approaches resulted in similar native defect formation energies and their charge state dependence; the results obtained here are within the range reported in the literature for different techniques. For example, this can be seen by comparing data in Fig. 8 with the corresponding states presented in Fig. 4 or Ref. [19], Fig. 1 in Ref. [20], and Fig. 1 in Ref. [5]. The energies obtained here are slightly higher than some published values; see, e.g., N-vacancy data in Fig. 3 here and Fig. 1 in Ref. [5]. The significantly larger supercell used here, i.e., 360 atoms, should provide a larger relaxation thus reducing the formation energy; however, this is compensated by the positive correction term E_{corr} in Eq. (1). Overall, previously published results and results obtained here have demonstrated similar accuracy of the applied approaches in calculating defect formation energies. Applying a large supercell should result in more accurate configurations and energies for interstitial and Frenkel pair defects modeled here.

A number of unique interstitial configurations observed in pure AlN are N and Al interstitial configurations and Sc as shown in Table III and Figs. 3, 4, 7, and 10. The most stable neutral Al and N interstitials were found to be the $[11\bar{2}1]$ dumbbell, $I1_{Al}$ and $I1_N$, respectively. However, the relative stability of different interstitial configurations depends on the manufacturing conditions and charge state as seen in Fig. 8. We have found only one description of interstitial atom configuration in AlN observed in [32] after relaxing small energy collision events at the neutral state using the SIESTA code. It was reported that N FPs always include the N interstitial in configuration $\langle 11\bar{2}1\rangle$ like the one considered here, $I1_N$ at the neutral state [see Table III and Fig. 3(a)], whereas Al primary knock-on atoms always produce Al interstitials in the octahedral configuration as observed here for Al-rich conditions [see Table III and Fig. 4(d)]. These, the most stable, interstitial configurations were used to model Al and N Frenkel pairs in this work.

Sc substitution in Al sites was found to be rather stable, see Table III and Fig. 6, and does not strongly affect the DOS as seen in Fig. 2. The interaction between two Sc atoms is weak and negative, implying impediment of the nucleation of Sc precipitates and thus predicting no clustering, at least, at dilute concentrations. However, Sc atoms affect the stability of different point defects. Thus Sc substituting for Al is far more stable than substituting N, as seen in Table III. Moreover, Sc substituting for Al does not affect the charge state. Irradiation conditions assume that defects are formed due to collision events and defect evolution under irradiation is not governed by thermodynamic conditions defined by defect formation energies. Instead, this is a result of kinetic processes due to interactions between mobile defects and existing microstructures and the defect binding energy is the main driving force of microstructure evolution under irradiation conditions. The binding energies considered here are among the basic necessary parameters for evaluating radiation effects in Sc-doped AlN. All binding energies calculated here at different charge conditions are presented in Fig. 10. Al vacancy repeals Sc atom, suggesting a weak effect of Sc to vacancy evolution and a weak vacancy contribution to Sc transport. N vacancy has positive binding energy with Sc, ~0.1–0.9 eV, which suggests a reduction of vacancy mobility and possible preferable nucleation of vacancy clusters near Sc dopants. Also, Sc can tightly bind both N and Al interstitials, thus reducing their mobility. Especially strong binding is observed with N interstitials near the CBM. Taking into account that N transport under irradiation is likely to occur by interstitial migration, this suggests preferential nucleation of N interstitial clusters around Sc dopants. This effect should be more profound at negative charge conditions.

Currently, there are no robust models that allow consideration of local states of defects, i.e., their Fermi energy and charge, and their effect on defect evolution under irradiation. In practice some additional assumptions are made to simplify the picture presented in Fig. 7. For example, in [59,60] for modeling defect evolution in UO_2 the defect Fermi levels were assumed to be at mid-band-gap. Applying the same approach here, this is around $E_F \sim 2$ eV. According to the data in Fig. 10, at this energy the main Sc effects are (a) repulsion with Al vacancy; (b) weak repulsion between Sc atoms; and (c) significant attraction to both N and Al interstitials.

V. CONCLUSIONS

In this work, we perfomed extended DFT modeling for different vacancy, substitution, and interstitial defects including small defect clusters (Frenkel pairs) that cover native and primary radiation induced defects in the wurtzite pristine AlN and Sc-doped AlN, materials relevant to sensor applications in nuclear reactor environments. Large supercell size and accounting for finite modeling cell size correction guaranteed accurate results on configurations and formation and binding energy estimations that are particularly important for interstitial and Frenkel pair defects. We presented a detailed description of the possible aluminum, nitrogen, and scandium interstitial atom configurations, and the charge effect to their configurations, formation, and binding energies is demonstrated. It was found that the most stable defects are neutral N and positively charged Al interstitial defects.

We estimated the binding energies of Sc-dopant atom with point defects, which are relevant for radiation damage processes, with the following main conclusions of the Sc-doping effects in defect energetics:

(1) Al vacancy repeals the Sc atom suggesting a generally weak effect of Sc to vacancy evolution and Sc transport by vacancy mechanism.

(2) N vacancy and both Al and N interstitials have attractive interaction with the Sc atom that reduces their mobility.

(3) Strong positive N interstitial interaction with Sc suggests preferential nucleation of N interstitial clusters associated with Sc substitutions.

(4) Sc doping stabilizes the Frenkel pairs by reducing their formation energy and increasing recombination radius.

(5) Weak repulsion between two Sc atoms preserves the formation of Sc precipitates.

Sc-doped AlN is a promising material for sensors in nuclear reactor environments that are subjected to high radiation. For predicting modeling of radiation response in this material at higher scale, further investigation of the defect properties, such as diffusion barriers, elastic properties, and their sensitivity to charge states is necessary.

ACKNOWLEDGMENTS

The authors acknowledge Dr. B. Uberuaga for fruitful discussions on the subject. Y.O., G.S., S.J.Z., and E.Z. are supported by the Laboratory Directed Research and Development Program of Oak Ridge National Laboratory, managed by UT-Battelle, LLC, for the U.S. Department of Energy. M.-H.D. was supported by the U.S. Department of Energy, Office of Science, Basic Energy Sciences, Materials Sciences and Engineering Division.

[1] F. A. Ponce and D. P. Bour, Nitride-based semiconductors for blue and green light-emitting devices, Nature (London) **386**, 351 (1997).

[2] Y. Taniyasu, M. Kasu, and T. Makimoto, An aluminium nitride light-emitting diode with a wavelength of 210 nanometres, Nature (London) **441**, 325 (2006).

[3] N. Sinha, G. E. Wabiszewski, R. Mahameed, V. V. Felmetsger, S. M. Tanner, R. W. Carpick, and G. Piazza, Piezoelectric aluminum nitride nanoelectromechanical actuators, Appl. Phys. Lett. **95**, 053106 (2009).

[4] H. Seo, M. Govoni, and G. Galli, Design of defect spins in piezoelectric aluminum nitride for solid-state hybrid quantum technologies, Sci. Rep. **6**, 20803 (2016).

[5] J. B. Varley, A. Janotti, and C. G. Van de Walle, Defects in AlN as candidates for solid-state qubits, Phys. Rev. B **93**, 161201(R) (2016).

[6] D. A. Parks and B. R. Tittmann, Radiation tolerance of piezoelectric bulk single-crystal aluminum nitride, IEEE Trans. Ultrason. Ferroelectr. Freq. Control **61**, 1216 (2014).

[7] D. Parks, Development of a piezoelectric ultrasonic array sensor for nuclear reactor applications, Ph.D. dissertation, Pennsylvania State University, 2012.

[8] Dal Corso, M. Posternak, R. Resta, and A. Baldereschi, *Ab initio* study of piezoelectricity and spontaneous polarization in ZnO, Phys. Rev. B **50**, 10715 (1994).

[9] K. Lorenz, M. Peres, N. Franco, J. G. Marques, S. M. C. Miranda, S. Magalhães, T. Monteiro, W. Wesch, E. Alves, and E. Wendler, Radiation damage formation and annealing in GaN and ZnO, Proc. SPIE **7940**, 79400O (2011).

[10] B. T. Reinhardt, A. Suprock, and B. Tittmann, Testing piezoelectric sensors in a nuclear reactor environment, in *43rd Annual Review of Progress in Quantitative Nondestructive Evaluation*, Vol. 36, AIP Conf. Proc. No. 1806 (AIP, Melville, NY, 2017), p. 050005.

[11] B. Reinhardt, J. Daw, and B. R. Tittmann, Irradiation testing of piezoelectric (aluminum nitride, zinc oxide, and bismuth titanate) and magnetostrictive sensors (remendur and galfenol), IEEE Trans. Nucl. Sci. **65**, 533 (2018).

[12] B. R. Tittmann, B. Reinhardt, and J. Daw, Introduction to special session on ultrasonic transducers for harsh environments, in *44th Annual Review of Progress in Quantitative Nondestructive Evaluation*, AIP Conf. Proc. No. 1949 (2018), p. 100001.

[13] O. Zywitzki, T. Modes, S. Barth, H. Bartzsch, and P. Frach, Effect of scandium content on structure and piezoelectric properties of AlScN films deposited by reactive pulse magnetron sputtering, Surf. Coatings Technol. **309**, 417 (2017).

[14] P. Daoust, P. Desjardins, R. A. Masut, V. Gosselin, and M. Côté, *Ab initio* piezoelectric properties of $Al_{0.5}Sc_{0.5}$ N: Impact of alloy

configuration on the $d_{33,f}$ piezoelectric strain coefficient, Phys. Rev. Mater. **1**, 055402 (2017).

[15] M. Akiyama, T. Kamohara, K. Kano, A. Teshigahara, Y. Takeuchi, and N. Kawahara, Enhancement of piezoelectric response in scandium aluminum nitride alloy thin films prepared by dual reactive cosputtering, Adv. Mater. **21**, 593 (2009).

[16] Y. Iwazaki, T. Yokoyama, T. Nishihara, and M. Ueda, Highly enhanced piezoelectric property of co-doped AlN, Appl. Phys. Express **8**, 061501 (2013).

[17] T. Yokoyama, Y. Iwazaki, Y. Onda, T. Nishihara, Y. Sasajima, and M. Ueda, Highly piezoelectric co-doped AlN thin films for wideband FBAR applications, IEEE Trans. Ultrason. Ferroelectr. Freq. Control **62**, 1007 (2015).

[18] Y. Kusano, G. Luo, D. Horsley, I. T. Ishii, and A. Teshigahara, 36% scandium-doped aluminum nitride piezoelectric micromachined ultrasonic transducers, *IEEE International Ultrasonics Symposium (IUS)* (IEEE, New York, 2018).

[19] C. Stampfl and C. G. Van de Walle, Theoretical investigation of native defects, impurities, and complexes in aluminum nitride, Phys. Rev. B **65**, 155212 (2002).

[20] Y. Zhang, W. Liu, and H. Niu, Native defect properties and *p*-type doping efficiency in group-IIA doped *wurtzite* AlN, Phys. Rev. B **77**, 035201 (2008).

[21] Q. Hu, T. Noda, H. Tanigawa, T. Yoneoka, and S. Tanaka, The oxygen-related defect complexes in AlN under gamma irradiation and quantum chemistry calculation, Nucl Instrum. Methods Phys. Res., Sect. B **191**, 536 (2002).

[22] M. Zdorovetsa, K. Dukenbayev, A. Kozlovskiy, and I. Kenzhina, Defect formation in AlN after irradiation with He^{2+} ions, Ceram. Int. **45**, 8130 (2019).

[23] T. Yano and T. Iseki, Swelling and microstructure of AlN irradiated in a fast reactor, J. Nucl. Mater. **203**, 249 (1993).

[24] M. Akiyoshi and T. Yano, Neutron-irradiation effect in ceramics evaluated from macroscopic property changes in as-irradiated and annealed specimens, Prog. Nucl. Energy **50**, 567 (2008).

[25] M. Akiyoshi, T. Yano, Y. Tachi, and H. Nakano, Saturation in degradation of thermal diffusivity of neutron-irradiated ceramics at 3×10^{26} n/m^2, J. Nucl. Mater. **367-370**, 1023 (2007).

[26] L. L. Snead, S. J. Zinkle, and D. P. White, Thermal conductivity degradation of ceramic materials due to low temperature low dose neutron irradiation, J. Nucl. Mater. **340**, 187 (2005).

[27] A. L. Kozlovskiy, D. I. Shlimas, I. E. Kenzhina, D. B. Borgekov, and M. V. Zdorovets, Dynamics of radiation damage in AlN ceramics under high-dose irradiation, typical for the processes of swelling and hydrogenation, Crystals **10**, 546 (2020).

[28] S. J. Zinkle, L. L. Snead, W. S. Eatherly, J. W. Jones, and D. K. Hensley, Effect of low temperature ion irradiation on the microstructure of nitride ceramics, in *Microstructural Processes During Irradiation*, edited by S. J. Zinkle, G. E. Lucas, R. C. Ewing, and J. S. Williams, Vol. 540 (Materials Research Society, Warrendale, PA, 1999), p. 305.

[29] S. J. Zinkle, Radiation-Induced Effects on Microstructure, in *Comprehensive Nuclear Materials*, 2nd ed., edited by R. J. M. Konings and R. E. Stoller (Elsevier, Oxford, 2020), Vol. 1, p. 91.

[30] S. O. Kucheyev, J. S. Williams, J. Zou, G. Li, C. Jagadish, M. O. Manasreh, M. Pophristic, S. Guo, and I. T. Ferguson, Structural disorder in ion-implanted $Al_xGa1_{-x}N$, Appl. Phys. Lett. **80**, 787 (2002).

[31] K. Atobe, M. Okada, and M. Nakagawa, Irradiation temperature dependence of defect formation of nitrides (AlN and *c*-BN) during neutron irradiations, Nucl. Instrum. Methods Phys. Res., Sect. B **166-167**, 57 (2000).

[32] J. Xi, B. Liu, Y. Zhang, and W. J. Weber, *Ab initio* molecular dynamics simulations of AlN responding to low energy particle radiation, J. Appl. Phys. **123**, 045904 (2018).

[33] W. Kohn and L. J. Sham, Self-consistent equations including exchange and correlation effects, Phys. Rev. **140**, A1133 (1965).

[34] J. P. Perdew, K. Burke, and M. Ernzerhof, Generalized Gradient Approximation Made Simple, Phys. Rev. Lett. **77**, 3865 (1996).

[35] P. E. Blöchl, Projector augmented-wave method, Phys. Rev. B **50**, 17953 (1994).

[36] Vienna *Ab Initio* Simulation Package, http://cms.mpi.univie.ac.at/vasp/.

[37] H. Schulz and K. H. Thieemann, Crystal structure refinement of AlN and GaN, Solid State Commun. **23**, 815 (1977).

[38] M. Tanaka, S. Nakahata, K. Sogabe, and H. Nakata, Morphology and x-ray diffraction peak widths of aluminum nitride single crystals prepared by the sublimation method, Jpn. J. Appl. Phys. **36**, L1062 (1997).

[39] V. L. Solozhenko and J. H. Edgar Properties of group III nitrides. EMIS Data-reviews Series N, **11**, 43 (1994).

[40] M. Fodil, A. Mounir, M. Ameri, H. Baltache, B. Bouhafs, Y. A. Douri, and I. Ameri, Structural and elastic properties of TiN and AlN compounds: First-principles study, Mater. Sci.-Pol. **32**, 220 (2014).

[41] Y. Gao, D. Sun, X. Jiang, and J. Zhao, Point defects in group III nitrides: A comparative first-principles study, J. Appl. Phys. **125**, 215705 (2019).

[42] A. F. Guillermet and G. Grimvall, Cohesive properties and vibrational entropy of 3*d* transition-metal compounds: *MX* (NaCl) compounds (X = C, N, O, S), complex carbides, and nitrides, Phys. Rev. B **40**, 10582 (1989).

[43] G. Makov and M. C. Payne, Periodic boundary conditions in *ab initio* calculations, Phys. Rev. B **51**, 4014 (1995).

[44] S. Lany and A. Zunger, Assessment of correction methods for the band-gap problem and for finite-size effects in supercell defect calculations: Case studies for ZnO and GaAs, Phys. Rev. B **78**, 235104 (2008).

[45] S. Lany and A. Zunger, Accurate prediction of defect properties in density functional supercell calculations, Modell. Simul. Mater. Sci. Eng. **17**, 084002 (2009).

[46] T. S. Moss, The interpretation of the properties of indium antimonide, Proc. Phys. Soc., Sect. B **67**, 775 (1954).

[47] E. Burstein, Anomalous optical absorption limit in InSb, Phys. Rev. **93**, 632 (1954).

[48] M.-H. Du, J. Yan, V. R. Cooper, and M. Eisenbach, Tuning Fermi levels in intrinsic antiferromagnetic topological insulators $MnBi_2Te_4$ and $MnBi_4Te_7$ by defect engineering and chemical doping, Adv. Funct. Mater. **31**, 2006516 (2021).

[49] Vurgaftman and J. R. Meyer, Band parameters for III–V compound semiconductors and their alloys, J. Appl. Phys. **89**, 5815 (2001).

[50] S. Lebegue, M. Klintenberg, O. Eriksson, and M. I. Katsnelson, Accurate electronic band gap of pure and functionalized graphene from *GW* calculations, Phys. Rev. B **79**, 245117 (2009).

[51] See Supplemental Material at http://link.aps.org/supplemental/10.1103/PhysRevB.93.161201 for details of the calculations and formation energies shown for both N-rich and Al-rich conditions.

[52] A. Hung, S. P. Russo, D. G. McCulloch, An *ab initio* study of structural properties and single vacancy defects in wurtzite AlN, J. Chem. Phys. **120**, 4890 (2004).

[53] G. D. Samolyuk, A. V. Barashev, S. I. Golubov, Y. N. Osetsky, and R. E. Stoller, Analysis of the anisotropy of point defect diffusion in hcp Zr, Acta Mater. **78**, 173 (2014).

[54] G. Verite, C. Domain, C.-C. Fu, P. Gasca, A. Legris, and F. Willaime, Self-interstitial defects in hexagonal close packed metals revisited: Evidence for low-symmetry configurations in Ti, Zr, and Hf, Phys. Rev. B **87**, 134108 (2013).

[55] K. Atobe, M. Honda, N. Fukuoka, M. Okada, and M. Nakagawa, F-type centers in neutron-irradiated AlN, Jpn. J. Appl. Phys. **29**, 150 (1990).

[56] F. B. Fara and V. Fiorentini, Theoretical evidence for the semi-insulating character of AlN, J. Appl. Phys. **85**, 2001 (1999).

[57] P. K. Bhala, G. K. H. Schwarz, D. Kvas-Nicka Madsen, and J. Luitz, *Computer code* WIEN2K (Vienna University of Technology, Vienna, 2002).

[58] Y. Hong-Gang, C. Guang-De, Z. You-Zhang, and L. Hui-Min, First principle study of nitrogen vacancy in aluminium nitride, Chin. Phys. **16**, 3803 (2007).

[59] D. A. Andersson, P. Garcia, X.-Y. Liu, G. Pastore, M. Tonks, P. Millett, B. Dorado, D. R. Gaston, D. Andrs, R. L. Williamson, R. C. Martineau, B. P. Uberuaga, and C. R. Stanek, Atomistic modeling of intrinsic and radiation-enhanced fission gas (Xe) diffusion in $UO_2 \pm x$: Implications for nuclear fuel performance modeling, J. Nucl. Mater. **451**, 225 (2014).

[60] C. Matthew, R. Perriot, M. W. D. Cooper, C. Stanek, and D. A. Anderson, Cluster dynamics simulation of uranium self-diffusion during irradiation in UO_2, J. Nucl. Mater. **527**, 151787 (2019).